SCIENTIFIC REPORTS

OPEN

SUBJECT AREAS:
INORGANIC CHEMISTRY
HETEROGENEOUS CATALYSIS

Received
7 April 2014

Accepted
23 May 2014

Published
11 June 2014

Correspondence and requests for materials should be addressed to P.L.C. (chenpl@iccas.ac.cn; cpl@zzu.edu.cn); T.S.L. (lts34@zzu.edu.cn) or M.H.L. (liumh@iccas.ac.cn)

* These authors contributed equally to this work.

Branched Au Nanostructures Enriched with a Uniform Facet: Facile Synthesis and Catalytic Performances

Mingshan Zhu[1]*, Bin Lei[1,2]*, Fangfang Ren[3], Penglei Chen[1,2], Yunfan Shen[1,2], Bo Guan[1], Yukou Du[3], Tiesheng Li[2] & Minghua Liu[1]

[1]Beijing National Laboratory for Molecular Science, CAS Key Laboratory of Colloid, Interface, and Chemical Thermodynamics, Institute of Chemistry, Chinese Academy of Sciences, Beijing 100190, P. R. China, [2]College of Chemistry and Molecular Engineering, Zhengzhou University, Zhengzhou, Henan 450001, P. R. China, [3]College of Chemistry, Chemical Engineering and Materials Science, Soochow University, Suzhou 215123, P. R. China.

Well–defined noble metal nanocrystals (NMNCs) of a unique morphology yet a uniform facet have attracted broad interests. In this regard, those with a highly branched architecture have gained particular attention. Most of the currently existing branched NMNCs, however, are enclosed by mixed facets. We now report that branched Au nanoarchitectures could be facilely fabricated by mixing an aqueous solution of $KAuCl_4$, an aqueous dispersion of graphene oxide, and ethanol under ambient conditions. Interestingly, unilike the conventional branched NMNCs, our unique Au nanostructures are predominately enriched with a uniform facet of {111}. Compared to the spherical Au nanostructures exposed with mixed facets, our branched nanospecies of a uniform facet display superior catalytic performances both for the catalytic reduction of 4–nitrophenol and the electrocatalytic oxidation of methanol. Our investigation represents the first example that Au nanostructures simultaneously featured with a highly branched architecture and a uniform crystal facet could be formulated. Our unique Au nanostructures provide a fundamental yet new scientific forum to disclose the correlation between the surface atomic arrangement and the catalytic performances of branched NMNCs.

Noble metal nanocrystals (NMNCs) of a size of 1 ~ 100 nm and a unique morphology have been the focus of much attention[1–9]. Among various NMNCs of a unique morphology, those with a branched architecture have attracted great interest[5,6,10–24]. This stems from their large surface–to–volume ratio, high surface roughness, and large number of multiple high angle edges and sharp tips[5,6,10–12]. These intrinsic features render them emerging candidates for high–performance advanced nanomaterials in a wide variety of fields, wherein those for nanocatalysts have gained particular attention[5,6,10,11,16–23]. Tremendous efforts have been devoted to branched NMNCs[5,6,10,11,16–23]. Most of the works focus on Pt, Pd, and bimetallic species, *etc.*[5,6,10–23], the paradigms concerning Au are relatively few[16,24], although there has currently been an increasing interest in Au nanoarchitectures due to their promising surface–sensitive uses[3,25–28].

Besides the intrinsic surface properties such as surface edges and tips, surface–to–volume ratio, and surface roughness, the exposed crystal facet is another crucial issue for surface–sensitive applications, especially for catalysts[1–6]. Numerous NMNCs enclosed by highly catalytically active facets have been developed[1–6]. In most of the cases, the nanocatalysts, however, are enclosed by mixed facets[1–6]. Actually, well–defined nanocatalysts predominantly exposed with a uniform facet are of great importance for modern advanced nanomaterials[1,2,29–33]. In contrast to those enclosed by mixed facets, they are simple systems. This enables them to be good model nanomaterials to disclose the correlation between surface atomic arrangement and properties. Moreover, by virtue of this feature, desired catalytic performances would be realized[1,2,30–37]. For example, it has been reported that the catalytic performance of the truncated octahedral Pt_3Ni increases with the increase in the fraction of {111} surface[34,35]. Very recently, it has been demonstrated that a high surface fraction of {111} facets exposed on the Pt–based multiply twinned nanoicosahedrons could lead to a superior catalytic activity[36].

So far, numerous highly branched NMNCs have been developed[4–6,10–23]. However, different from the above examples of nanopolyhedrons, it still remains a formidable challenge to construct NMNCs simultaneously featured with a branched architecture and a uniform crystal facet. We herein report a facile one–pot synthesis of 3D branched Au nanostructures simply by mixing a $KAuCl_4$ aqueous solution, a graphene oxide (GO) aqueous

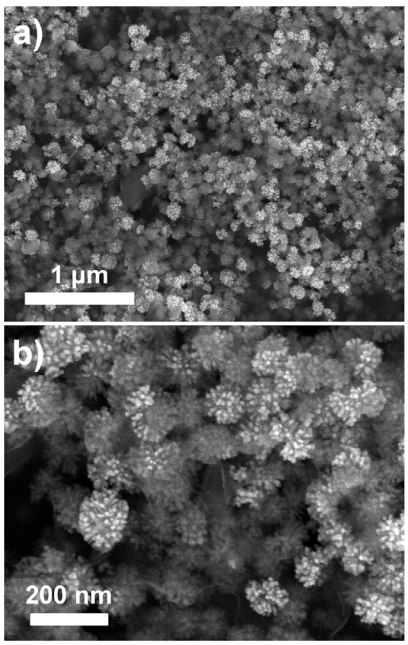

Figure 1 | Typical low–magnification SEM (a) and high–magnification SEM (b) images of our branched Au nanostructures.

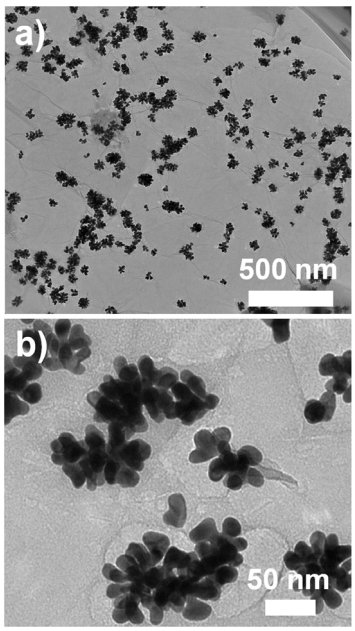

Figure 2 | Typical low–magnification (a) and high–magnification (b) TEM images of our branched Au nanostructures.

dispersion, and ethanol under ambient conditions. Excitingly, unlike the traditional highly branched NMNCs, our unique Au nanoarchitectures are predominantly enriched with a uniform crystal facet of {111}. Compared to the Au nanospheres of a similar dimension and of a mixed crystal facet, our branched Au nanostructures of a uniform facet exhibit superior catalytic performances not only for the reduction of 4–nitrophenol (4–NP), but also for the electrocatalytic oxidation of methanol. Our results represent the first report that highly branched Au nanoarchitectures of a uniform crystal facet could be formulated. Our well–defined branched Au species, which are enriched with a uniform facet, provide a fundamental yet new scientific forum to correlate the surface atomic arrangement and catalytic performances of branched noble metal nanocatalysts.

Results

Typically, an aqueous GO dispersion and ethanol were dropwise added into an aqueous solution of $KAuCl_4$. The obtained yellowish dispersion was aged at 25 ~ 30°C for 5 days. During this process, the dispersion became dark yellowish gradually. The nanostructures were washed fully with Milli–Q water by means of centrifugation or filtration. The morphology of the nanostructures was examined by scanning electron microscopy (SEM). As illustrated in Figure 1a, the typical SEM image measured over large area surface indicates that almost all the nanoparticles have a 3D branched morphology, which exhibit nearly a spherical profile. The average size of these nanostructures is *ca.* 100 nm. A close observation of the high–magnification SEM image (Figure 1b) indicates that owing to the presence of lots of branches, the nanostructures display a rough surface. Besides, translucent GO nanosheets featured with a wrinkled morphology could also be observed evidently.

Figure 2 shows the representative transmission electron microscopy (TEM) images of our nanostructures at different magnifications. The low–magnification TEM images (Figure 2a) clearly indicate the presence of wrinkled GO nanospecies, on which branched Au nanospecies are distributed. These observations preliminarily suggest the existence of GO nanosheets in the as–formulated samples, in which Au nanostructures might hybridize with GO nanosheets. This could be further experimentally confirmed by the EDX elemental analysis, XPS spectra, and FT–IR spectra of the samples shown in Figure S1, S2 and S3, respectively. On the other hand, high–magnification TEM image (Figure 2b) confirms that the as–synthesized Au nanoarchitectures are composed of many arms. The average size of each arm is *ca.* 20 nm. Note that an apparent contrast between the peripheral branches and the cores could be observed, verifying their 3D feature.

To obtain deep insights into the crystallinity and lattice facets presented in our Au nanoarchitectures, their structures were further examined by means of powder X–ray diffraction (PXRD). As shown in Figure 3A, the PXRD pattern displays a strong yet sharp diffraction peak (2θ) at *ca.* 38.2° and a weak peak at *ca.* 44.4°. These peaks could be indexed to the characteristic diffractions from the {111} and {200} facets of the face–centered–cubic (fcc) Au (JCPDS No. 4–0784), respectively[10,38,39]. An interplanar spacing of *ca.* 0.235 and 0.204 nm, respectively, could be derived from these two peaks. It is interesting to note that the intensity ratio of the {200} peak to the {111} peak, estimated using {111} as a reference (that is, 1), is *ca.* 0.125. This value is substantially smaller (specifically speaking, nearly 4 times) than that reported in the standard JCPDS file of Au, which generally is *ca.* 0.5[10,38,39]. The observation of this exceptionally prominent {111} peak preliminarily indicates that our branched Au nanostructures are predominantly enriched with {111} crystal facets. Commonly, in the standard JCPDS file of fcc Au, the intensity ratio of the {220} and {311} peaks to the {111} peak is *ca.* 0.32 and 0.36, respectively[38,39]. In our case, it can be seen that the diffraction peaks ascribing to the {220} and {311} lattice facets are quite weak such that they could not be well discerned (Figure 3A), leading to an absolutely smaller intensity ratio of the {220} and {311} peaks to the {111} peak. The nearly undiscernible diffraction peaks attributing to the {220} and {311} lattice planes and the surprisingly prominent {111} peak further verify the extremely high population of {111} planes in our samples. The PXRD pattern of our nanostructures was also measured after the samples were kept for about 6 months. As shown in Figure 3A and S4, there is only slight change in their PXRD pattern. This indicates that our branched Au nanostructures enriched with {111} facets are stable species.

To further verify the dominate population of {111} planes in our branched nanostructures, their high–resolution TEM (HRTEM) images were measured. As shown in Figure 3B and 3C, evident lattice fringes indicating a lattice spacing of *ca.* 0.235 nm, which correspond

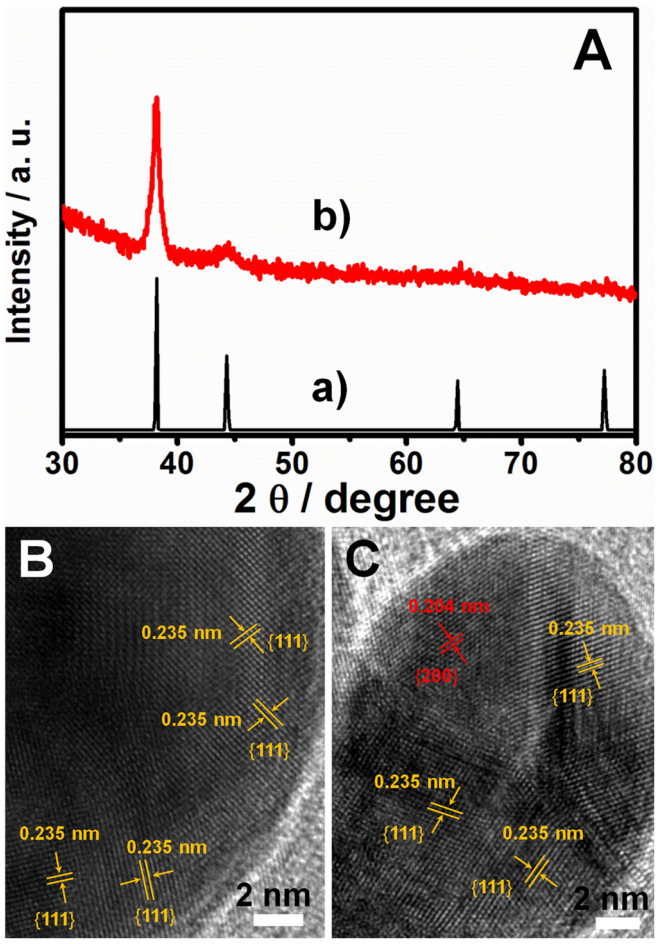

Figure 3 | (A): PXRD pattern of the (a) poly–Au (JCPDS No. 4–0784), and (b) the as–prepared branched Au nanostructures. (B) and (C): Typical HRTEM images of the as–prepared branched Au nanostructures.

to the {111} facets of Au, could be easily observed in a high population in the representative HRTEM images. Meanwhile, lattice fringes with a lattice spacing of *ca.* 0.204 nm, corresponding to the {200} planes of Au, could also be detected occasionally in a small fraction. Experimentally, we found that the lattice fringes ascribing to other lattice facets, such as {220} and {311}, could hardly be observed. It is worth pointing out that the HRTEM images of the samples were measured at the different regions of the same or different nanospecies chosen randomly, and the measurements were carried out tens of times. Roughly similar results were obtained in all the cases. These observations are in good agreement with the facts obtained from the PXRD investigations, further confirming that our branched Au nanostructures are predominantly enriched with {111} facets.

Our facile one–pot synthesis of branched Au nanostructures was performed in the presence of GO nanosheets. To disclose the role played by GO, controlled experiments in the absence of GO were also carried out. As illustrated in Figure S5, when no GO nanosheets were presented in the synthesis system, only ill–defined irregular Au nanoparticles could be obtained. Together with the above–mentioned results shown Figure 1 and 2, these facts reveal that GO nanosheets are of crucial importance for the formation of our branched Au nanoarchitectures.

As known, GO is geometrically an atomic thick nanosheet of two–dimensional honeycomb lattice of carbon atoms whose basal planes and edges are engrafted with various oxy–functional groups, such as carboxyl, hydroxyl, epoxide, *etc*[40–42]. The presence of these oxygen functionalities endows GO nanosheets with negative surface charges[42], and more importantly, provides them with abundant reactive sites for the construction of GO–based hybrid nanocomposites[40–43]. As verified in terms of zeta potential measurements, our GO nanosheets are negatively charged with a zeta potential of *ca.* −40.8 mV. On the other hand, for the synthesis of Au–hybridized nanostructures using $AuCl_4^-$ as Au source and GO or oxygen groups containing polymers as scaffold, the $AuCl_4^-$ species would generally interact with the oxy–functional groups in terms of the Au^{3+} cation *via* partial replacement of Cl^- ligands[43,44]. Thus, the electrostatic, coordination or dipole interactions between oxygen functionalities and Au^{3+} cations would lead to a localized enrichment of Au^{3+} cations around these oxy–functional groups. The result is that these oxygen–containing functional groups would work as implantation sites for an *in situ* nucleation and a subsequent growth of Au nanoparticles during the ethanol–assisted Au^{3+} reduction[24,43]. The evolution process of our branched Au nanostructures was monitored by examining the TEM images of the nanostructures formed at a desired stage, as presented in Figure 4. When the aging time was 0 minute, only translucent GO nanosheets, decorated without any nanoparticles, could be observed. In contrast, when the synthesis system was aged for 30 minutes, GO nanosheets grafted with numerous tiny nanoparticles of *ca.* 2 ∼ 5 nm, were observed. This indicates the initiation of Au nucleation, and it suggests that the oxygen functionalities of the GO nanosheets indeed act as implantation sites during the ethanol–assisted Au^{3+} reduction.

Interestingly, when the aging time was extended to 60 minutes, the population of the tiny nanoparticles of *ca.* 2 nm formed at the former stage decreased distinctly, while that of *ca.* 5 nm could only be observed occasionally. At the same time, it is important to note that some bigger nanostructures of *ca.* 10 ∼ 15 nm, which exhibit a primitive morphology of branched nanostructure, could also be observed. When the aging time was further prolonged to 12 and 48 hours, the crude branched nanospecies formed in the previous stage gradually become bigger and gain a preliminary morphology of branched structure. Meanwhile, some tiny nanostructures with a size of *ca.* 2 ∼ 5 nm appeared at this stage again. Finally, when the aging time was extended to 5 days, well–defined branched architectures with a size of *ca.* 100 nm came into being together with a disappearance of the formerly observed small nanoparticles. It can be seen that the appearance and growth of the branched species are always accompanied by an iterative appearance/disappearance of tiny nanoparticles. These observations indicate a simultaneous occurrence of ethanol–assisted Au^{3+} reduction and Ostwald ripening (a disappearance of tiny nanospecies accompanied by a gradual growth of the bigger ones), which eventually leads to the formation of perfect branched Au nanoarchitectures.

Experimentally, well–defined branched Au nanostructures could only be produced when the synthesis system was aged for 5 days. On one hand, at such a low growth rate, the nanocrystals would experience a relaxation process, wherein the adatoms would migrate on the surface of the crystals so as to minimize the total surface energy[6]. On the other hand, as it is known, among the facets of the fcc crystals, {111} planes exhibit the lowest surface energy[3,45]. As a result, the as–formulated branched nanostructures are predominantly enriched with {111} facets. Note that the syntheses of our branched Au nanospecies were performed under ambient conditions of a temperature of *ca.* 25 ∼ 30°C. Controlled experiments at a lower (∼10°C) and higher (∼50°C) temperature were also carried out to gain deep insights into the synthesis. As illustrated in Figure 5, only ill–defined irregular nanospecies of *ca.* 20 and 40 nm but no branched nanostructures are produced, respectively, under these conditions. These facts indicate that our branched nanoarchitectures obtained under ambient conditions are formed *via* a diffusion limited growth model[24]. Owing to microscopic irregularities on the surface of the seed nanoparticles, they grow up anisotropically with the tips

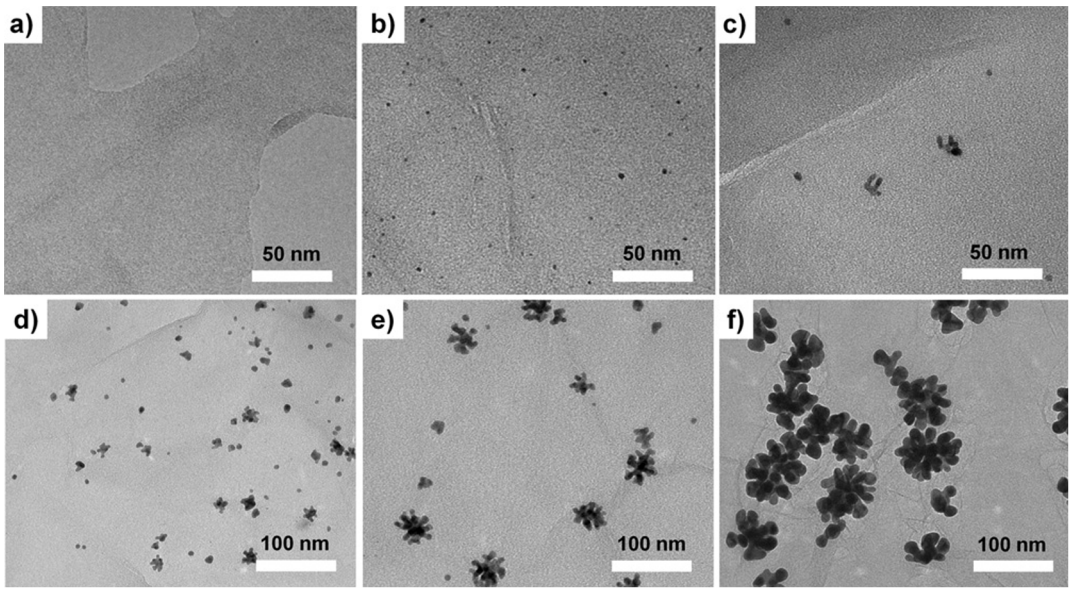

Figure 4 | Real–time TEM images of the samples formulated at a desired stage. The aging time is 0 min (a), 30 min (b), 60 min (c), 12 h (d), 48 h (e), and 5 days (f), respectively.

growing preferentially, resulting in the formation of branched nanoarchitectures[24].

As known, 4–aminophenol (4–AP) is an important chemical reagent widely used in numerous applications, including analgesic and antipyretic drugs, photographic developer, corrosion inhibitor, anticorrosion lubricant, *etc*[46,47]. The production of 4–AP could be achieved by a reduction of 4–nitrophenol (4–NP) using $NaBH_4$ and noble metals as reducing agents and catalysts, respectively[38,46,47]. As a preliminary example to demonstrate the possible advantages of our branched Au nanostructures of a uniform crystal facet, their catalytic performances toward the reduction of 4–NP were investigated. To make a reasonable comparison, we synthesized Au nanospheres of *ca.* 20 nm (similar to the size of an arm of our branched Au nanostructures, abbreviated as Au–S20, hereafter) and of *ca.*100 nm (similar to the total size of one branched structure, abbreviated as Au–S100, hereafter) in the presence of GO nanosheets (Figure S6–S8). As shown in Figure S6, the obtained Au nanospheres are exposed with various mixed crystal facets. These Au nanospheres were used as the reference catalysts. The catalytic performances were monitored by measuring the real–time UV–vis spectra of the reaction system. As shown in Figure S9A, negligible changes are observed from the UV–vis spectra when no catalysts but only 4–NP and $NaBH_4$ are involved in the reaction system. This indicates an inefficient reduction of 4–NP by $NaBH_4$ under our experimental conditions (Figure 6A and 6B).

On the other hand, when our Au–S100 and Au–S20 are introduced into the reaction system, the UV–vis spectra display a successive decrease at the absorption peak of 400 nm and a concomitant increase of a new absorption at 300 nm (Figure S9B and S9C). This suggests that 4–NP could be catalytically reduced to 4–AP by our Au nanospheres[38,45]. As summarized in Table 1 and illustrated in Figure 6A and 6B, *ca.* 50.4% and *ca.* 84.7% 4–NP molecules were reduced to 4–AP within 16 minutes by Au–S100 and Au–S20, respectively. There is a nice linear correlation between $\ln(C_t/C_0)$ and the reduction time, suggesting that the catalytic reduction reaction follows a pseudo–first–order kinetic. A rate constant (k) of *ca.* 0.045 min^{-1} and *ca.* 0.081 min^{-1} could be estimated from the slope of the linear correlation. This is indicative of the size effect of our Au nanospheres based catalysts, wherein the smaller the catalysts, the higher the catalytic performances. Interestingly, when our branched Au nanostructures are introduced into the reaction system, the absorptions at 400 and 300 nm lose and gain their intensity quickly with elapsed time, respectively (Figure S9D). As illustrated in Figure 6A and 6B, the reduction reaction could be achieved nearly 100% within 16 minutes. In this case, a rate constant of *ca.* 0.233 min^{-1} could be obtained. This value is almost 5.2 times and 2.9 times of that of the reaction systems catalyzed by Au–S100 and Au–S20, respectively. These facts indicate that compared to Au–S100 and Au–S20 of a mixed crystal facet, our branched nanostructures of

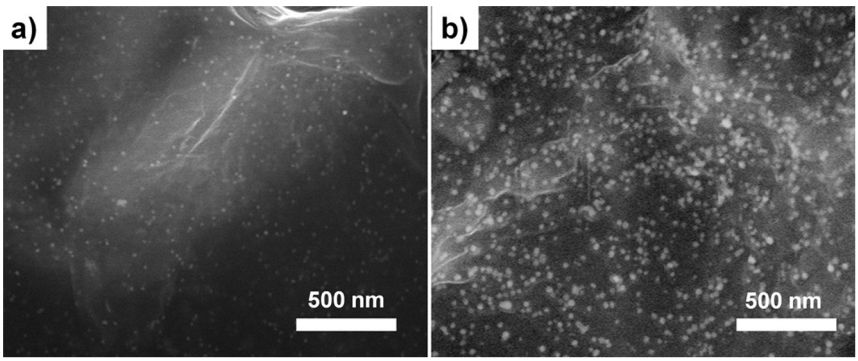

Figure 5 | Typical SEM images of the ill–defined irregular Au nanoparticles synthesized at ~10°C (a) and ~50°C (b) in the presence of GO nanosheets.

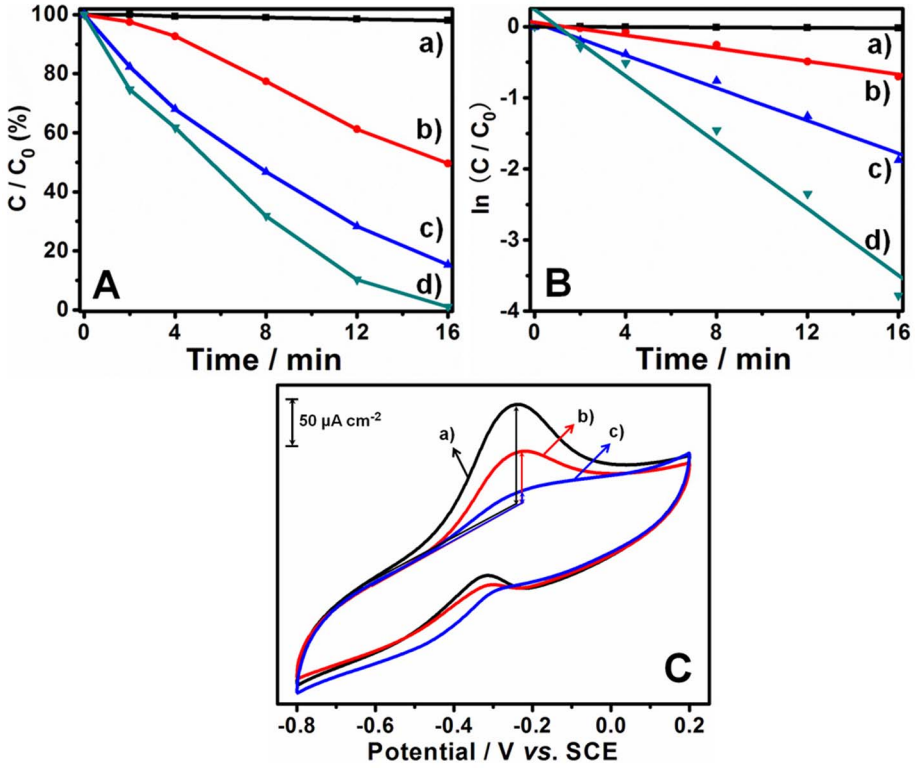

Figure 6 | Catalytic performances (A) and kinetic linear simulation curves (B) of our catalysts for the reduction of 4–NP, (a): no catalyst; (b) ~ (d): Au-S100, Au-S20 and branched Au nanostructures are used as catalysts, respectively. (C): CV scans of our branched Au nanostructures (a), Au-S20 (b) and Au-S100 (c) modified electrodes in a mixed soulation of 1 M KOH and 1 M CH_3OH with a potential scan rate of 50 mV s^{-1} under ambient conditions.

a uniform facet could work as superior catalysts for the reduction of 4–NP to 4–AP.

As summarized in Table 1, the normalized rate constant (k_n) of our catalysts, which is obtained by normalizing the rate constant (k) values with respect to the total amount (mmol) of the used catalysts, is deduced. Meanwhile, the turnover frequency (TOF) of our catalysts were also calculated and presented in Table 1. It can be seen that among Au-S100, Au-S20, and our branched Au nanoarchitectures, the latter displays the highest k_n and TOF values. These results further indicate that compared to the formers, our branched Au nanostructures are superior catalysts toward the reduction of 4–NP.

Moreover, the k_n of our catalysts was also compared to that reported by others[38]. Two typical catalysts in reference 38, namely, sample A of a size of *ca.* 4 ~ 13 nm with enriched {111} facets, and sample C of a size of *ca.* 11 ~ 20 nm enclosed by mixed facets, are chose to make a comparison. We deduce that the k_n of sample A and C therein is approximately 19.9 and 0.22 $mmol^{-1}$ s^{-1}, respectively. It can be seen that the k_n of our branched Au is about 2.2 time larger than that of sample C, although the size of sample C is smaller than that of each arm of our branched Au structures. This suggests that {111} facet might contribute to the relatively higher catalytic performances of our branched nanospecies. Besides, it can be seen that our branched Au displays smaller k_n compared to sample A of an enriched {111} facet. This could be owing to the fact that the size of sample A is substantially smaller than that of the arm of our branched Au structures. As a matter fact, compared to the smaller ones (4 ~ 6 nm), heterocatalysts of a big size have their own advantages such as easy separation from the reaction medium, potential recovery for recycling, *etc*. Considering this issue, we suggest that our branched Au nanoarchitectures might have a bright future for potential applications, although compared to the smaller Au nanoparticle of an enriched {111} facet, they display inferior catalytic reactivity.

Ballarin, Cassani and coworkers have recently shown that the catalytic performances of Au nanoparticles–containing membranes toward the reduction of 4–NP could display a distinct enhancement with the increase of the {111} crystal planes[38]. This is attributed to the fact that among the crystal facets of fcc crystals, the atomic arrangement in {111} planes displays the highest atomic planar density[38,48].

Table 1 | A summarization of the catalytic performances of our Au–based naoncatalysts toward the catalytic reduction of 4–NP and electrocatalytic oxidation of CH_3OH at room temperature

Catalyst	Conversion percentage[a)]	Kinetic constant (min^{-1})[a)]	Normalized rate constant (mmol s^{-1})[a)]	Turnover frequency (TOF, h^{-1})[a)]	Current density ($\mu A\ cm^{-2}$)[b)]	Peak potential (V)[b)]
no catalyst	2%	0.001	2×10^{-3}	–	–	–
branched Au nanostructures	100%	0.233	0.48	0.26	103	−0.24
Au–S20	84.7%	0.081	0.17	0.22	55.3	−0.22
Au–S100	50.4%	0.045	0.093	0.13	13.2	−0.22

[a)]: catalytic reduction of 4–NP to 4–AP;
[b)]: electrocatalytic oxidation of CH_3OH.

On one hand, as verified by the aforementioned experimental facts that in comparison with the Au–S100 and Au–S20 of a mixed crystal facet, our branched Au nanostructures are predominantly enriched with {111} facets. This could contribute partially to their superior catalytic performances. On the other hand, as known, the unique branched morphological features of nanodendrites endow them with a large number of multiple high angle edges and sharp tips, a large surface–to–volume ratio, and a high surface roughness, which favor a superior catalytic performance[5,6,10–12]. We suggest that this factor might also contribute partially to their superior catalytic performances.

As known, besides the well–known catalytic reduction of 4–NP, nanostructured Au species could also work as catalysts for the electrocatalytic oxidation of methanol[25,49–53], which is of fundamental importance to fuel cell catalysis[54,55]. This significant electrocatalytic oxidation reaction is recognized to be of crucial significance for the development of modern catalysis used in fuel cell, which is a key enabling technology for a direct conversion of chemical energy to electrical energy with high efficiency and low emission of pollutants[54,55]. The electrocatalytic performances of the above–mentioned three kinds of Au nanostructures were also investigated in terms of the electrocatalytic oxidation of methanol in alkaline media at room temperature. The measurement of the cyclic voltammograms (CV) of our catalysts was performed within a potential range of $-0.8 \sim 0.2$ V and a scan rate of 50 mV s^{-1} in a mixed solution of 1 M KOH and 1 M CH_3OH, as shown in Figure 6C.

For electrocatalytic activity evaluation, the values of the forward methanol oxidation current density and of the corresponding peak potential are summarized in Table 1. It can be seen that the current density of the methanol oxidation on our branched Au nanostructures modified electrode is *ca.* 103 μA cm^{-2}. This value is *ca.* 1.9 and 7.8 times larger than that of the electrodes modified by Au–S20 (*ca.* 55.3 μA cm^{-2}) and Au–S100 (*ca.* 13.2 μA cm^{-2}), respectively. On the other hand, it can be seen that when our branched Au nanoarchitectures are used as electrocatalysts, a peak potential of *ca.* −0.24 V could be obtained. This value is negatively shifted by *ca.* 0.02 V compared to the *ca.* −0.22 V of the Au–S20 and Au–S100. This is owing to the enrichment of the {111} facets in our branched Au nanostructures[50–53]. Nevertheless, together with the above–mentioned results obtained from the catalytic reduction of 4–NP, these electrocatalytic results strongly suggest that compared to Au–S100 and Au–S20, which are exposed with mixed crystal facets, our well–defined branched nanostructures, which are predominantly enriched with {111} facets, are superior nanocatalysts. The synergistic effect of their abundant {111} crystal facets and their unique branched morphological features might play an important role.

In summary, branched Au nanoarchitectures of *ca.* 100 nm are successfully fabricated under ambient conditions by means of a facile, green, one–pot protocol using GO nanosheets as directing reagent. Different from the conventional branched NMNCs, our unique branched Au nanostructures are predominantly enriched with {111} facets. Compared to the Au nanospheres of various mixed facets and of a similar dimension, our unique branched Au nanostructures display superior catalytic performances. The cooperative effect of their unique branched nature and their enriched {111} facets might contribute much to these interesting catalytic behaviors.

Methods

Materials. Potassium tetrachloroaurate (III) hydrate ($KAuCl_4$, Alfa Aesar, 99%), graphite powder (Alfa Aesar, 325mesh, 99.9995%), 4–nitrophenol (4–NP, Beijing Chemical Reagents Plant, A. R.). Sodium borohydride ($NaBH_4$), A. R. grade methanol (CH_3OH) and potassium hydroxide (KOH) were purchased form Sinopharm Chemical Reagent Co., Ltd. All of samples were used as received without further treatment.

Instruments. The scanning electron microscopy (SEM) measurements were carried out using a Hitachi S–4800 system. The energy dispersive X–ray spectroscopy (EDX) was measured with a Horiba EMAX X–act energy dispersive spectroscopy that was attached to the Hitachi S–4800 system. The transmission electron microscopy (TEM) of the nanomaterials was measured with a JEOL–2100F, which was operated with an accelerating voltage of 200 kV. X–ray diffraction (XRD) measurements were performed on a PANalytical X'Pert PRO instrument with Cu Kα radiation. The catalytic reduction of 4–NP was monitored by measuring the real–time UV–vis spectra of the catalytic systems using a Hitachi U–3010 spectrometer. JASCO IR–660 spectrometer was employed for the FT–IR spectral measurements. X–ray photoelectron spectroscopy (XPS) was performed on an ESCALab220i–XL electron spectrometer from VG Scientific using 300 W Al Kα radiation. The binding energies were referenced to the C1s line at 284.8 eV from adventitious carbon. Zeta potential measurements of our GO aqueous solutions were performed using a Zetasizer Nano ZS ZEN3600 (Malvern) instrument. All the measurements were carried out under ambient conditions.

Synthesis. *Preparation of graphene oxide (GO) nanosheets.* GO nanosheets were synthesized through a chemical exfoliation of graphite powder by using a modified Hummers' method. The detailed synthesis was carried out according to the procedures described previously[56].

Synthesis of branched Au nanostructures. In a typical process, a 2 mL aqueous dispersion of GO nanosheets (1 mg mL^{-1}), 4 mL ethanol and 200 μL $KAuCl_4$ (1×10^{-3} mol L^{-1}) aqueous solution were added dropwise into a 14.8 mL water. The mixture was aged at $25 \sim 30$°C for 5 days, after which the as–formulated nanostructures were collected and washed fully with Milli–Q water by means of repeating high–speed centrifugation (12000 rpm, 15 minutes). To monitor the formation of the branched Au nanostructures, the reaction was terminated by means of filtration at a desired stage. After being fully washed with Milli–Q water, the samples were investigated by means of TEM. On the other hand, the synthesis system could also be aged at ~10°C and ~50°C. In these cases, only ill–defined irregular nanospecies of *ca.* 20 and 40 nm but no branched nanostructures were produced, respectively.

Synthesis of Au nanospheres with a size of 20 nm (Au–S20) and 100 nm (Au–S100) in the presence of GO nanosheets. First, Au nanospheres with a size of 20 nm were synthesized *via* a modified Frens method[57], wherein a $KAuCl_4$ aqueous solution (0.5 mL, 1 wt%) and a GO aqueous dispersion (500 μL, 1 mg mL^{-1}) were added to a citrate aqueous solution (1.5 mL, 1 wt%) under stirring. This mixture was quickly poured into boiling water (48 mL), after which the reaction system was further refluxed for 30 minutes for the formation of uniform spherical Au nanoparticles of a size of 20 nm. The as–prepared dispersion of Au nanosphere was subsequently cooled to room temperature. The products were collected and washed fully with Milli–Q water by means of repeating high–speed centrifugation (12000 rpm, 15 minutes).

Au nanospheres with a size of 100 nm were prepared using a seeding growth method[58] in the presence of GO nanosheets. Typically, a GO aqueous dispersion (500 μL, 1 mg mL^{-1}), a $KAuCl_4$ aqueous solution (4.95 mL, 6 μM), and a citrate aqueous solution (25 μL, 1 wt%) were mixed together, into which 5 mL H_2O_2 (30 wt%) was immediately poured under stirring at a speed of *ca.* 1000 rpm. Then, the prefabricated dispersion of Au nanospheres with a size of 20 nm (30 μL) was injection into this mixture under ambient conditions. The color of the reaction system changed from slight yellow to purple within 5 minutes, suggesting the formation of Au nanospheres. The products were collected and washed fully with Milli–Q water by means of repeating high–speed centrifugation (12000 rpm, 15 minutes).

Catalytic performances toward the catalytic reduction of 4–NP. The catalytic performances were carried out using a quartz cell (1 cm path length) as reactor. Typically, freshly prepared aqueous solution of $NaBH_4$ (0.4 mL, 0.08 M) and 4–nitrophenol (4–NP) aqueous solution (0.4 mL, 1.4 mM) were added into 1.8 mL water, leading to a color change from light yellow to yellow–green. Then, 1 mL aqueous dispersion of our catalysts (*ca.* 1.6 mg) was added into this mixture under stirring. The real–time UV–vis spectra of the reaction system were measured to monitor the progress of the catalytic reaction. For the evaluation of the catalytic activities, C is the concentration of 4–NP molecules at a real–time t, and C_o is the concentration of 4–NP solution before the introduction of catalysts.

Fabrication of electrodes and electrocatalytic performances. For the electrochemical experiments, the electrode was fabricated by a modification of glassy carbon (GC, 3 mm diameter) electrode using our branched Au nanostructures, Au–S20 or Au–S100. Before modification, the GC electrode surface was polished with 0.3 μm alumina slurry, and then rinsed with water in an ultrasonic bath. Subsequently, suspension of our Au nanostructures (30 μL, *ca.* 0.04 mg) was dropped on the surface of the GC electrode and dried under ambient condition.

The electrochemical experiments were carried out in a three–electrode cell using a CHI 660B potentiostat/galvanostat (Shanghai Chenhua Instrumental Co., Ltd., China) at room temperature. GC electrodes modified by our Au nanostructures were used as working electrode. The counter electrode and the reference electrode were platinum wire and saturated calomel electrode (SCE), respectively. Electrolyte solutions were deaerated by a dry nitrogen stream and maintained under slight nitrogen over pressure during the experiments. In order to study the electrocatalytic activity, the oxidation of CH_3OH on the Au nanostructuers modified GC electrodes was examined in a mixed aqueous solution (saturated with N_2) of 1.0 M KOH and 1.0 M CH_3OH. The current density was used for the evaluation of the electrocatalytic activity, which was calculated from the ratio of the peak current and the surface area of GC electrodes.

1. Zhou, K. & Li, Y. Catalysis based on nanocrystals with well–defined facets. *Angew. Chem. Int. Ed.* **51**, 602–613 (2012).
2. Wang, D., Xie, T. & Li, Y. Nanocrystals: solution–based synthesis and applications as nanocatalysts. *Nano Res.* **2**, 30–46 (2009).
3. Xiao, J. & Qi, L. Surfactant–assisted, shape–controlled synthesis of gold nanocrystals. *Nanoscale* **3**, 1383–1396 (2011).
4. Xia, Y., Xiong, Y., Lim, B. & Skrabalak, S. E. Shape–controlled synthesis of metal nanocrystals: simple chemistry meets complex physics? *Angew. Chem. Int. Ed.* **48**, 60–103 (2009).
5. Li, S. Y. & Wang, M. Branched metal nanoparticles: a review on wet–chemical synthesis and biomedical applications. *Nano LIFE* **02**, 1230002 (2012).
6. Lim, B. & Xia, Y. Metal nanocrystals with highly branched morphologies. *Angew. Chem. Int. Ed.* **50**, 76–85 (2011).
7. Cui, C.-H. & Yu, S.-H. Engineering interface and surface of noble metal nanoparticle nanotubes toward enhanced catalytic activity for fuel cell applications. *Acc. Chem. Res.* **46**, 1427–1437 (2013).
8. Gong, J., Li, G. & Tang, Z. Self–assembly of noble metal nanocrystals: fabrication, optical property, and application. *Nano Today* **7**, 564–585 (2012).
9. Gao, M.-R., Xu, Y.-F., Jiang, J. & Yu, S.-H. Nanostructured metal chalcogenides: synthesis, modification, and applications in energy conversion and storage devices. *Chem. Soc. Rev.* **42**, 2986–3017 (2013).
10. Huang, X. *et al*. Palladium–based nanostructures with highly porous features and perpendicular pore channels as enhanced organic catalysts. *Angew. Chem. Int. Ed.* **52**, 2520–2524 (2013).
11. Ma, L. *et al*. Control over the branched structures of platinum nanocrystals for electrocatalytic applications. *ACS Nano* **6**, 9797–9806 (2012).
12. DeSantis, C. J. & Skrabalak, S. E. Core values: elucidating the role of seed structure in the synthesis of symmetrically branched nanocrystals. *J. Am. Chem. Soc.* **135**, 10–13 (2012).
13. Mahmoud, M. A., Tabor, C. E., El–Sayed, M. A., Ding, Y. & Wang, Z. L. A new catalytically active colloidal platinum nanocatalyst: the multiarmed nanostar single crystal. *J. Am. Chem. Soc.* **130**, 4590–4591 (2008).
14. Wang, L. & Yamauchi, Y. Block copolymer mediated synthesis of dendritic platinum nanoparticles. *J. Am. Chem. Soc.* **131**, 9152–9153 (2009).
15. Lacroix, L.-M. *et al*. Tuning complex shapes in platinum nanoparticles: from cubic dendrites to fivefold stars. *Angew. Chem. Int. Ed.* **51**, 4690–4694 (2012).
16. Mohanty, A., Garg, N. & Jin, R. A universal approach to the synthesis of noble metal nanodendrites and their catalytic properties. *Angew. Chem. Int. Ed.* **49**, 4962–4966 (2010).
17. Xia, B. Y., Ng, W. T., Wu, H. B., Wang, X. & Lou, X. W. Self–supported interconnected Pt nanoassemblies as highly stable electrocatalysts for low–temperature fuel cells. *Angew. Chem. Int. Ed.* **51**, 7213–7216 (2012).
18. Lim, B. *et al*. Pd–Pt bimetallic nanodendrites with high activity for oxygen reduction. *Science* **324**, 1302–1305 (2009).
19. Wang, L., Nemoto, Y. & Yamauchi, Y. Direct synthesis of spatially–controlled pt–on–pd bimetallic nanodendrites with superior electrocatalytic activity. *J. Am. Chem. Soc.* **133**, 9674–9677 (2011).
20. Peng, Z. M. & Yang, H. Synthesis and oxygen reduction electrocatalytic property of Pt–on–Pd bimetallic heteronanostructures. *J. Am. Chem. Soc.* **131**, 7542–7543 (2009).
21. Yeo, K. M., Choi, S., Anisur, R. M., Kim, J. & Lee, I. S. Surfactant–free platinum–on–gold nanodendrites with enhanced catalytic performance for oxygen reduction. *Angew. Chem. Int. Ed.* **50**, 745–748 (2011).
22. Xu, J. G. *et al*. Synthesis and catalytic properties of Au–Pd nanoflowers. *ACS Nano* **5**, 6119–6127 (2011).
23. Guo, S. J., Dong, S. J. & Wang, E. K. Three–dimensional Pt–on–Pd bimetallic nanodendrites supported on graphene nanosheet: facile synthesis and used as an advanced nanoelectrocatalyst for methanol oxidation. *ACS Nano* **4**, 547–555 (2010).
24. Jasuja, K. & Berry, V. Implantation and growth of dendritic gold nanostructures on graphene derivatives: electrical property tailoring and Raman enhancement. *ACS Nano* **3**, 2358–2366 (2009).
25. Daniel, M. C. & Astruc, D. Gold nanoparticles: assembly, supramolecular chemistry, quantum–size–related properties, and applications toward biology, catalysis, and nanotechnology. *Chem. Rev.* **104**, 293–346 (2004).
26. Hashmi, A. S. K. Gold–catalyzed organic reactions. *Chem. Rev.* **107**, 3180–3211 (2007).
27. Zhang, Y., Cui, X. J., Shi, F. & Deng, Y. Q. Nano–gold catalysis in fine chemical synthesis. *Chem. Rev.* **112**, 2467–2505 (2012).
28. Zhu, H., Ke, X., Yang, X., Sarina, S. & Liu, H. Reduction of nitroaromatic compounds on supported gold nanoparticles by visible and ultraviolet light. *Angew. Chem. Int. Ed.* **49**, 9657–9661 (2010).
29. Qi, L. Colloidal chemical approaches to inorganic micro– and nanostructures with controlled morphologies and patterns. *Coord. Chem. Rev.* **254**, 1054–1071 (2010).
30. Yang, D. *et al*. An efficient photocatalyst structure: TiO_2(B) nanofibers with a shell of anatase nanocrystals. *J. Am. Chem. Soc.* **131**, 17885–17893 (2009).
31. Yang, D. *et al*. Capture of radioactive cesium and iodide ions from water by using titanate nanofibers and nanotubes. *Angew. Chem. Int. Ed.* **50**, 10594–10598 (2011).
32. Tian, N., Zhou, Z.-Y., Sun, S.-G., Ding, Y. & Wang, Z. L. Synthesis of tetrahexahedral platinum nanocrystals with high–index facets and high electro–oxidation activity. *Science* **316**, 732–735 (2007).
33. Zhao, X. *et al*. Shape– and size–controlled synthesis of uniform anatase TiO_2 nanocuboids enclosed by active {100} and {001} facets. *Adv. Funct. Mater.* **21**, 3554–3563 (2011).
34. Wu, J. *et al*. Truncated octahedral Pt_3Ni oxygen reduction reaction electrocatalysts. *J. Am. Chem. Soc.* **132**, 4984–4985 (2010).
35. Stamenkovic, V. R. *et al*. Improved oxygen reduction activity on Pt_3Ni (111) via increased surface site availability. *Science* **315**, 493–497 (2007).
36. Yang, J., Yang, J. & Ying, J. Y. Morphology and lateral strain control of Pt nanoparticles via core–shell construction using alloy AgPd core toward oxygen reduction reaction. *ACS Nano* **6**, 9373–9382 (2012).
37. Zhou, X. *et al*. Facet–mediated photodegradation of organic dye over hematite architectures by visible light. *Angew. Chem. Int. Ed.* **51**, 178–182 (2012).
38. Ballarin, B. *et al*. Gold nanoparticle–containing membranes from in situ reduction of a gold(III)−aminoethylimidazolium aurate salt. *J. Phys. Chem. C* **114**, 9693–9701 (2010).
39. Lin, T.-H., Lin, C.-W., Liu, H.-H., Sheu, J.-T. & Hung, W.-H. Potential–controlled electrodeposition of gold dendrites in the presence of cysteine. *Chem. Commun.* **47**, 2044–2046 (2011).
40. Dreyer, D. R., Park, S., Bielawski, C. W. & Ruoff, R. S. The chemistry of graphene oxide. *Chem. Soc. Rev.* **39**, 228–240 (2010).
41. Kim, J., Cote, L. J. & Huang, J. X. Two dimensional soft material: new faces of graphene oxide. *Acc. Chem. Res.* **45**, 1356–1364 (2012).
42. Zhu, M., Chen, P. & Liu, M. High–performance visible–light–driven plasmonic photocatalysts Ag/AgCl with controlled size and shape using graphene oxide as capping agent and catalyst promoter. *Langmuir* **29**, 9259–9268 (2013).
43. Yin, H. J., Tang, H. J., Wang, D., Gao, Y. & Tang, Z. Y. Facile synthesis of surfactant–free Au cluster/graphene hybrids for high–performance oxygen reduction reaction. *ACS Nano* **6**, 8288–8297 (2012).
44. Tripathy, P., Ram, S. & J.-Fecht, H. Gold nanoparticles from induced $Au^{3+} \rightarrow Au^0$ reaction in polyvinyl alcohol molecules in presence of sucrose in hot water. *Plasmonics* **1**, 121–127 (2006).
45. Wang, C., Markovic, N. M. & Stamenkovic, V. R. Advanced platinum alloy electrocatalysts for the oxygen reduction reaction. *ACS Catal.* **2**, 891–898 (2012).
46. Saha, S., Pal, A., Kundu, S., Basu, S. & Pal, T. Photochemical green synthesis of calcium–alginate–stabilized Ag and Au nanoparticles and their catalytic application to 4–nitrophenol reduction. *Langmuir* **26**, 2885–2893 (2010).
47. Herves, P. *et al*. Catalysis by Metallic Nanoparticles in Aqueous Solution: Model Reactions. *Chem. Soc. Rev.* **41**, 5577–5587 (2012).
48. Ghali, E. Corrosion resistance of aluminum and magnesium alloys: understanding, performance, and testing. John Wiley & Sons, Inc, Hoboken, New Jersey (2010).
49. Luo, J. *et al*. Thermal activation of molecularly–wired gold nanoparticles on a substrate as catalyst. *J. Am. Chem. Soc.* **124**, 13988–13989 (2002).
50. Lin, T.-H., Lin, C.-W., Liu, H.-H., Sheu, J.-T. & Hung, W.-H. Potential–controlled electrodeposition of gold dendrites in the presence of cysteine. *Chem. Commun.* **47**, 2044–2046 (2011).
51. Avramov–Ivić, M., Jovanović, V., Vlajnić, G. & Popić, J. The electrocatalytic properties of the oxides of noble metals in the electro–oxidation of some organic molecules. *J. Electroanal. Chem.* **423**, 119–124 (1997).
52. Borkowska, Z., Tymosiak–Zielinska, A. & Shul, G. Electrooxidation of methanol on polycrystalline and single crystal gold electrodes. *Electrochim. Acta* **49**, 1209–1220 (2004).
53. Jena, B. K. & Raj, C. R. Synthesis of flower–like gold nanoparticles and their electrocatalytic activity towards the oxidation of methanol and the reduction of oxygen. *Langmuir* **23**, 4064–4070 (2007).
54. Steele, B. C. H. & Heinzel, A. Materials for fuel–cell technologies. *Nature*, **414**, 345–352 (2001).
55. Aricò, A. S., Bruce, P., Scrosati, B., Tarascon, J.-M. & van Schalkwijk, W. Nanostructured materials for advanced energy conversion and storage devices. *Nature Mater.* **4**, 366–377 (2005).
56. Zhu, M., Chen, P. & Liu, M. Graphene oxide enwrapped Ag/AgX (X = Br, Cl) nanocomposite as a highly efficient visible–light plasmonic photocatalyst. *ACS Nano* **5**, 4529–4536 (2011).
57. Frens, G. Controlled nucleation for the regulation of the particle size in monodisperse gold suspensions. *Nature* **241**, 20–22 (1973).
58. Liu, X. K., Xu, H. L., Xia, H. B. & Wang, D. Y. Rapid seeded growth of monodisperse, quasi–spherical, citrate–stabilized gold nanoparticles *via* H_2O_2 reduction. *Langmuir* **28**, 13720–13726 (2012).

Acknowledgments

We appreciate NSFC (21372225, 20873159, 21021003, 21227802, and 91027042), National Key Basic Research Project of China (2011CB932301 and 2013CB834504), and CAS (XDA09030200, and 1731300500015). The authors also thank Dr. Chuncheng Chen, and Wanhong Ma from Institute of Chemistry, Chinese Academy of Sciences, for their helpful revision on English.

Author contributions

M.Z. and B.L. performed synthetic and catalytic reduction of 4–NP experiments. F.R. and Y.D. conducted electrocatalytic experiments. B.G. and Y.S. performed and discussed TEM

results. P.C., T.L. and M.L. were responsible for providing guidance for the experiments. All authors discussed the results. P.C. wrote the paper. All authors reviewed the manuscript. M.Z and B.L. contributed equally to this work.

Additional information

Supplementary information accompanies this paper at http://www.nature.com/scientificreports

Competing financial interests: The authors declare no competing financial interests.

How to cite this article: Zhu, M.S. *et al.* Branched Au nanostructures enriched with a uniform facet: facile synthesis and catalytic performances. *Sci. Rep.* **4**, 5259; DOI:10.1038/srep05259 (2014).

This work is licensed under a Creative Commons Attribution-NonCommercial-ShareAlike 4.0 International License. The images or other third party material in this article are included in the article's Creative Commons license, unless indicated otherwise in the credit line; if the material is not included under the Creative Commons license, users will need to obtain permission from the license holder in order to reproduce the material. To view a copy of this license, visit http://creativecommons.org/licenses/by-nc-sa/4.0/